JGR Solid Earth

RESEARCH ARTICLE
10.1029/2021JB023106

The Helium Elemental and Isotopic Compositions of the Earth's Core Based on Ab Initio Simulations

Liang Yuan[1] **and Gerd Steinle-Neumann**[1]

[1]Bayerisches Geoinstitut, Universität Bayreuth, Bayreuth, Germany

Key Points:

- We perform ab initio calculations showing that helium is lithophile but becomes increasingly compatible with metal at deep mantle conditions
- The core has a low helium elemental abundance (~4.2 ng/g) but possibly maintains a high primordial 3He/4He ratio (~140 times atmospheric)
- The core potentially plays a key role in serving as a reservoir for He sampled by ocean island basalts with high 3He/4He ratios

Supporting Information:

Supporting Information may be found in the online version of this article.

Correspondence to:

L. Yuan,
liang.yuan@uni-bayreuth.de

Citation:

Yuan, L., & Steinle-Neumann, G. (2021). The helium elemental and isotopic compositions of the Earth's core based on ab initio simulations. *Journal of Geophysical Research: Solid Earth*, *126*, e2021JB023106. https://doi.org/10.1029/2021JB023106

Received 25 AUG 2021
Accepted 4 OCT 2021

Abstract We use density functional theory-based molecular dynamics simulations to predict the partitioning behavior of helium (He) between coexisting metal and silicate melts at conditions of the magma ocean and the current core–mantle boundary. Helium strongly favors silicate over metal at low pressures and temperatures (10 GPa and 3,000 K) but it becomes approximately two orders of magnitude more compatible with metal at greater pressures and temperatures (50 GPa and 4,000 K) expected in a deep magma ocean. We further examine He partitioning behavior for varying metal compositions (pure Fe, Fe-S, and Fe-O alloys) and find that oxygen enhances He incorporation into the core by one to two orders of magnitude. The He elemental and isotopic compositions of the Earth's core are estimated to be ~4.2 ng/g and ~140 atmospheric ^{3}He/^{4}He ratio assuming the core containing some amounts of oxygen as required to explain the core density deficit. Our results suggest that the core may play a key role as a reservoir for the He signature recorded in ocean island basalts with distinctively high ^{3}He/^{4}He ratios.

Plain Language Summary The Earth's core has been suggested to be a long-term host for the isotope ^{3}He that must be preserved from the formation of the Earth more than 4 billion years ago. This ^{3}He isotope is shown to be present in ocean island basalts (for example Hawaii or Iceland) in an amount that is untypical for other basalts that form the ocean floor. Using advanced quantum mechanical modeling, we show that, although He favors silicate over metallic melts at high pressure and temperature, conditions under which Earth's core formed, the core possibly maintains a high primordial ^{3}He content relative to ^{4}He. Therefore, the core may play a significant role as a deep-rooted source enriched in ^{3}He for the ocean island basalts.

1. Introduction

Helium is continuously transferred from the solid Earth to the atmosphere by magmatic degassing and subsequently lost to space by gravitational escape (Pepin & Porcelli, 2002). The α-decay of uranium (U) and thorium (Th) replenishes mantle ^{4}He, but ^{3}He is almost exclusively primordial in origin (i.e., incorporated during accretion) and, as a consequence, mantle convection and plate tectonics result in a decrease of the ^{3}He/^{4}He ratio in all geochemical reservoirs over time (Jackson et al., 2010). This rate depends on the ^{3}He/(U + Th) ratio, and distinct He reservoirs exist, for example, with high ^{3}He/^{4}He ratios of 8–50 R_a (where R_a is the atmospheric ratio) for basalts (Stuart et al., 2003) and $\ll 1\ R_a$ for continental crust due to the depletion of U (and Th) relative to He in mantle residue produced by melting events (Parman, 2007; Parman et al., 2005). Therefore, helium isotopes (^{3}He and ^{4}He) play a central role in the study of mantle structure and evolution (Farley & Neroda, 1998; Graham, 2002; Mukhopadhyay & Parai, 2019).

Ocean island basalts (OIB) from major hotspot volcanoes, such as Hawaii and Iceland, can have higher ratios of ^{3}He/^{4}He by a factor of six compared to mid-ocean ridge basalts (MORB) that form from melting of the upper mantle (Kurz et al., 1983; Parai et al., 2012; Stuart et al., 2003). The high ^{3}He/^{4}He ratios identified in OIB have been broadly interpreted as sampling a relatively undegassed reservoir in the deep Earth (Allègre et al., 1983; Kurz et al., 1982), although a possible early depletion in U and Th (Parman, 2007; Parman et al., 2005) questions the presence of such enriched mantle reservoirs.

Hypotheses suggest that high ^{3}He/^{4}He lavas are fed by plumes originating from relatively undegassed primitive domains in the lower mantle (Allègre et al., 1983; Hart et al., 1992; Kellogg et al., 1999) or the D″ layer (Coltice & Ricard, 1999; Macpherson et al., 1998; Tolstikhin & Hofmann, 2005), with links established to the large low shear-wave velocity provinces (Williams et al., 2019) and the ultralow-velocity zones (Mundl-Petermeier et al., 2017, 2020), or to residual melts of a basal magma ocean (Herzberg et al., 2013). However, key questions regarding the longevity of isolated mantle reservoirs over planetary timescales remain unresolved as mantle

heterogeneities tend to be stirred and homogenized by convection (van Keken et al., 2002; M. Li & McNamara, 2013). Geophysical (Van Der Hilst et al., 1997), and geochemical (Albarède, 2008) evidence indicates material recycling into the lower mantle, implying that most of Earth's mantle should have been processed by partial melting, leaving the mantle extensively He-outgassed.

Alternatively, the core has been invoked as a source for the He isotopic ratios of OIB (Bouhifd, Jephcoat, et al., 2013; Porcelli & Halliday, 2001; Roth et al., 2019; Trieloff & Kunz, 2005). This scenario is supported by considerable evidence (Brandon et al., 1998; Herzberg et al., 2013; Humayun, 2004; Rizo et al., 2019) indicating that Earth's core contributes to the OIB geochemical signature; in particular, low $^{182}W/^{184}W$ values reported for Icelandic lavas (Mundl-Petermeier et al., 2020) seem to require a core contribution, and OIB $^{3}He/^{4}He$ ratios may be influenced in a similar fashion. On the other hand, Scherstén et al. (2004) failed to resolve the $^{182}W/^{184}W$ isotope anomalies of several Hawaiian picrites, negating a core contribution in their source; further, no discernable core signature is seen through the W/U ratio of the Hawaiian basaltic sources (Arevalo & McDonough, 2008).

Any core influence on the OIB $^{3}He/^{4}He$ budget would require a significant amount of He to be incorporated into the core during core–mantle segregation, which hinges on the partitioning of He between metallic and silicate melt at high pressure (P) and temperature (T), with only a few relevant experiments performed (Bouhifd, Jephcoat, et al., 2013; Matsuda et al., 1993). Bouhifd, Jephcoat, et al. (2013) investigated He partitioning and solution behavior over a P range of 0–16 GPa using diamond anvil cells (DACs). In agreement with previous experiments using the large-volume press at $P < 10$ GPa (Matsuda et al., 1993), they found that He mainly resides in the silicate, but even with a small metal–silicate partition coefficient, the Earth's early core could still have incorporated significant quantities of He, and as such, the possibility that core He contributes to the characteristic isotopic ratios of OIB cannot be ruled out. However, significant challenges and limitations in current high P–T experiments include:

(i) Metal–silicate equilibrium conditions during core–mantle segregation are expected to be $P \sim 40$–60 GPa and $T > 3{,}500$ K (Siebert et al., 2012), while experimental He-partitioning data are only available at moderate P–T, that is, <16 GPa and <2,600 K (Bouhifd, Jephcoat, et al., 2013). Therefore, understanding the distribution of He in the deep magma ocean has to rely on significant extrapolations of experimental data, where their validity remains untested.
(ii) Compositional analysis is carried out on samples quenched from high P–T to ambient conditions. The strong decrease of He solubility with P potentially leads to He loss during the rapid drop in P, an interpretation that is supported by the observation of He incorporation in SiO_2 glass at high P even at room T by in-situ synchrotron experiments (Sato et al., 2011; Shen et al., 2011), but its absence in the recovered sample.
(iii) Helium was not only used as a starting material but also as a P-transmitting medium in Bouhifd, Jephcoat, et al. (2013), resulting in a partial P of He of tens of GPa, orders of magnitude greater than during core formation in the early Earth. Crystals may contain trapped helium in extended defects or micro/nano-inclusions (Watson & Cherniak, 2003) in such a He-rich atmosphere at high T, resulting in very high apparent solubilities (Burnard et al., 2015; Wartho et al., 2005).
(iv) High reactivity between iron and carbon at high T requires samples to be insulated from the diamond anvils to avoid carbon contamination (Prakapenka et al., 2003; Rouquette et al., 2008). Despite the use of He as a P-transmitting medium in the experiments by Bouhifd, Jephcoat, et al. (2013) the sample is likely in contact with the diamond anvils, and may therefore contain carbon (Aprilis et al., 2019); its influence on He partitioning remains untested.
(v) High $^{3}He/^{4}He$ ratios reflect high time-integrated $^{3}He/(U + Th)$ ratios. Metal–silicate partitioning data on U and Th over a wide range of P–T conditions have become available in recent years (Blanchard et al., 2017; Bouhifd, Andrault, et al., 2013; Boujibar et al., 2019; Faure et al., 2020; Wohlers & Wood, 2015, 2017). Yet no systematic study has compared He and U (and Th) partitioning to explore the $^{3}He/^{4}He$ fingerprint of the core.

Recently, Xiong et al. (2021) computed He partition coefficients between pure Fe and $MgSiO_3$ melts using molecular dynamics (MD) simulations based on density functional theory (DFT). Their results support the core to be a host for primordial He. However, these simulations were only performed at a high T of 5,000 K. Here it is our goal to examine in detail the scenario of He incorporation into the Earth's core by modeling He-bearing metallic and silicate melts to determine He partitioning over a wide range of P–T conditions (10–130 GPa and

2500–5,000 K, Figure S1 in Supporting Information S1) that are directly comparable to those of metal–silicate equilibration during core formation (Siebert et al., 2012). We put a focus on quantifying the He partitioning behavior for varying metal compositions (pure Fe, Fe-S, and Fe-O alloys) as required to explain the core density deficit (Badro et al., 2014). Helium partition coefficients computed from our DFT-MD simulations, combined with previous U (and Th) partitioning data, are included in single-stage and continuous models of core formation to constrain the He budget and isotopic composition of the core.

2. Computational Methods

We perform first-principles electronic structure calculations based on Kohn-Sham (KS) DFT in the generalized gradient approximation (GGA) (Perdew et al., 1996) and the plane-wave pseudopotential method using the Vienna *ab initio* simulation package (VASP) (Kresse & Hafner, 1993; Kresse & Furthmüller, 1996). Electronic KS-DFT states are computed at the Brillouin zone center with a basis-set energy cutoff of 450 eV. Born–Oppenheimer MD simulations are performed in the canonical ensemble using the Nosé–Hoover thermostat (Hoover, 1985; Nosé, 1984) and run for >20 ps with a time step of $\Delta t = 1$ fs. The liquid state of the structures is confirmed by inspecting the mean-square displacement (MSD) for each atom type and partial radial distribution functions $g(r)$ between them.

We use two-phase simulations to qualitatively understand He partitioning behavior. They model element partitioning directly as the two phases are put in direct contact (Figure S2) (Yuan & Steinle-Neumann, 2020), which resembles experiments. Initial configurations prepared for our two-phase simulations are generated by carrying out independent DFT-MD simulations on single-phase He-bearing silicate and metallic liquids at comparable P and identical T of the thermostat. Metal and silicate configurations are then combined into a single slab. Details of simulated P–T conditions, melt compositions, and cell dimensions are tabulated in Table S1. Similar heterogenous phase simulation techniques have been widely used to obtain a variety of thermodynamic properties in the framework of DFT, including melting T (Alfè, 2005, 2009, 2005; Schwegler et al., 2008; Usui & Tsuchiya, 2010), thermal conductivity (Pulighedu et al., 2017; Pulighedu & Galli, 2020), and silicate vaporization (Xiao & Stixrude, 2018).

We compute the Helmholtz (F) and Gibbs (G) energies of silicate and metallic liquids by thermodynamic integration to quantitatively determine the He metal–silicate partition coefficient $D^{m/s}$, which is defined by the ratio of mass fractions of He in metal and silicate. Standard DFT-MD simulations only provide internal energy and pressure, but not entropy of the system. Therefore we use DFT-MD combined with the thermodynamic integration method to obtain F and G (e.g., Alfè et al., 2000; Vočadlo et al., 2008; Wahl & Militzer, 2015; Xiong et al., 2018). We perform a direct thermodynamic integration from the ideal gas to the fully DFT interacting system at fixed volumes and temperatures (Dorner et al., 2018; Rang & Kresse, 2019; Taniuchi & Tsuchiya, 2018; Xiong et al., 2018). We use the following reactions to evaluate He partitioning between the metallic (pure Fe, Fe-O, and Fe-S alloys) and silicate melts

$$\left(MgSiO_3\right)_{15} He + Fe_{50} \leftrightarrow \left(MgSiO_3\right)_{15} + Fe_{50}He, \tag{1a}$$

$$\left(MgSiO_3\right)_{15} He + Fe_{40}O_{10} \leftrightarrow \left(MgSiO_3\right)_{15} + Fe_{40}O_{10}He, \tag{1b}$$

$$\left(MgSiO_3\right)_{15} He + Fe_{45}S_5 \leftrightarrow \left(MgSiO_3\right)_{15} + Fe_{45}S_5He. \tag{1c}$$

We compute G of each phase in these reactions and obtain their Gibbs energy change ($\Delta_r G$). The equilibrium constant of He defined in terms of the mole concentrations of He in the metallic and silicate melts can then be calculated as

$$K_D = \exp\left(\frac{-\Delta_r G}{k_B T}\right), \tag{2}$$

where k_B is the Boltzmann constant. Further details of the computations are included in Supporting Information S1.

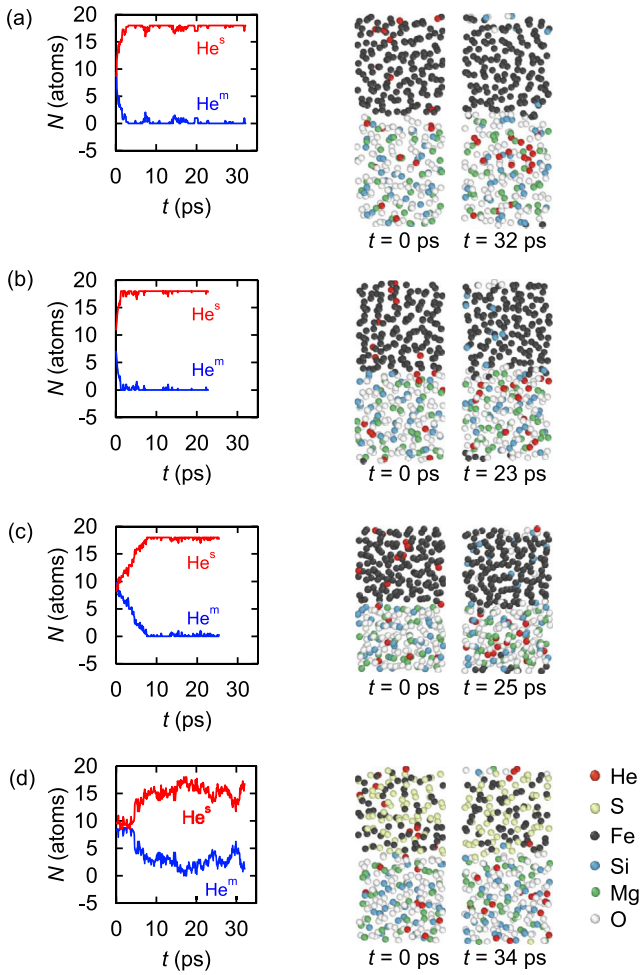

Figure 1. (left) Time-evolution of the two-phase simulation showing the number (N) of helium atoms in the silicate (He^s) and metallic (He^m) liquids for $Fe_{150}He_9$–$Mg_{35}Si_{35}O_{105}He_9$ at (a) 10 GPa and 2,496 K, (b) 38 GPa and 2,994 K, (c) 127 GPa and 3,788 K, and for (d) $Mg_{35}Si_{35}O_{105}He_9$–$Fe_{60}S_{60}He_9$ at 35 GPa and 2993 (k) (right) Initial and final configurations of the simulations, animations for the development of the cells can be found in the supporting online material (SI, Movie S1).

3. Results

3.1. Two-Phase Simulation

Initial configurations for two-phase simulations consist of arrangements of nine He atoms each located in the silicate (He^s) and metallic (He^m) liquids. The time-evolution of the number of He atoms in the two coexisting liquids with snapshots of the initial and final configurations of the two-phase simulation results are shown in Figure 1 (Table S1; animations for the development of the simulation cell can be found as Movie S1). For pure Fe as the metallic liquid, we observe the diffusion of He atoms from iron to the silicate at all P–T conditions considered (Figures 1a–1c), leading to an accumulation of He in the silicate melt which is documented by the time-development of their number in the two phases. The number of He^s becomes immediately larger than that of He^m; all He^m atoms transfer into the silicate phase within 2 ps at low–medium P–T conditions (i.e., 10 GPa and 2,496 K, and 38 GPa and 2,994 K), and within 7 ps at high P–T conditions (i.e., 127 GPa and 3,788 K).

The two-phase simulations in the Fe-S alloy–silicate system (Figure 1d and Movie S1d) confirm the lithophile nature of He. However, few He atoms remain in the Fe-S alloy over the entire simulation period of ~34 ps which is reflected by the stronger fluctuation in the He number profiles (Figure 1d; Movie S1d) compared to the pure Fe systems (Figures 1a–c). Detailed modeling of the Fe-S alloy at other P–T conditions and consideration of other metal alloys are beyond the scope of this study, especially given the limitations of the two-phase approaches (i) these simulations are computationally very demanding due to the large cell sizes, and (ii) they provide only qualitative information of partitioning. We rather focus our attention on quantifying $D^{m/s}$ of He over a wide range of P–T–composition using thermodynamic integration (Section 3.3).

The MSD of all atomic species (Figure S3) shows that He is more mobile than the host atoms in the melts by more than one order of magnitude, with the computed self-diffusivity sequence of $\alpha_{He} > \alpha_{Fe} > \alpha_S > \alpha_O \geq \alpha_{Mg} > \alpha_{Si}$ for all conditions considered–due to the small mass of He and its little to no interactions with other species. The α_{Fe} in the sulfur-bearing system is larger than in the sulfur-free system, whereas α_{Si} and α_O in the former are slightly smaller than in the latter at similar P–T conditions. The differences of α_{Fe}, α_{Si}, and α_O in two systems can be caused by two factors: (i) The transport of host atoms can be enhanced by sulfur, as demonstrated in previous DFT-MD work (Posner & Steinle-Neumann, 2019); (ii) statistical variations of self-diffusivity from a single DFT-MD trajectory can reach 40% (He et al., 2018; Yuan et al., 2020).

The fast dynamics of He compared to the host atoms that comprise silicate (Si, Mg, and O) and metal (Fe) is critical for our two-phase simulations as it ensures that He atoms reach their equilibrium positions rapidly in two coexisting phases, but prohibits extensive mixing between the two liquids at T of this study (2,500–3,800 K). The mobility of heavy host atoms is enhanced substantially with increasing T, which leads to complete mixing of silicate (or silica) and metallic liquids, as observed in previous DFT-MD simulations in the Fe-Si-O ternary at >3,800 K and 136 GPa (Huang et al., 2019).

The self-diffusivity of He and supercell lengths of the pure iron (38 GPa, 2,994 K, $Fe_{150}He_9$–$Mg_{35}Si_{35}O_{105}He_9$) and the sulfur-bearing systems (35 GPa, 2,993 K, $Fe_{60}S_{60}He_9$–$Mg_{35}Si_{35}O_{105}He_9$) are comparable (Figures 1b and 1d; Table S1), whereas the simulation time for completion of He transfer from metal to silicate in the sulfur-bearing system is 10 times larger than that in the sulfur-free system (20 vs. 2 ps). This less efficient redistribution of He in the sulfur-bearing system is therefore uncorrelated with hampered kinetics but suggests that He is thermodynamically favored to stay in iron-sulfide melt relative to pure iron when coexisting with a silicate

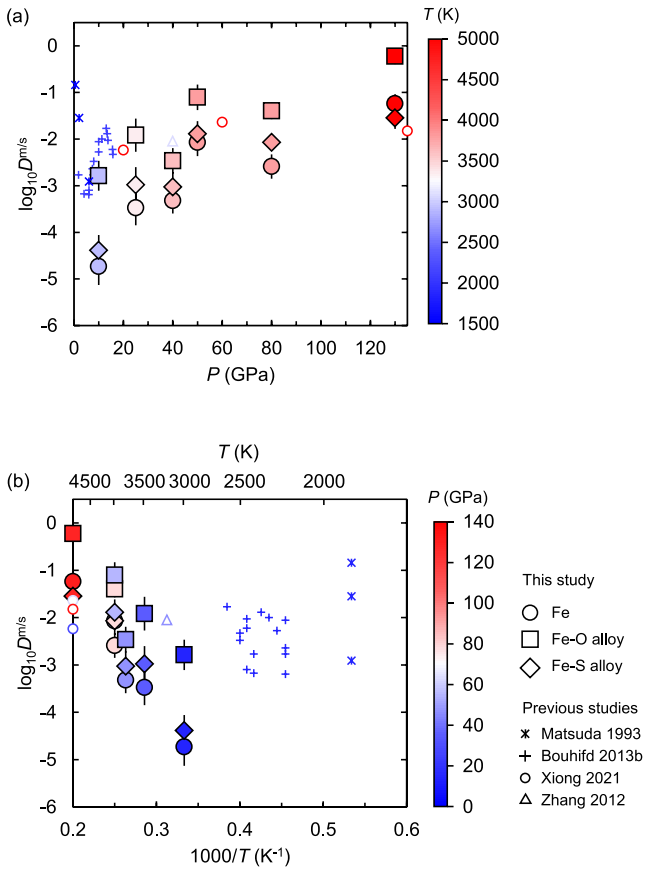

Figure 2. Calculated partition coefficients between metallic and silicate melts $D^{m/s}$ as a function of (a) pressure (P) and (b) temperature (T). Results of this study are shown as large symbols with filled colors representing temperatures/pressures: Fe–$MgSiO_3$ (circles); Fe-O alloy–$MgSiO_3$ (squares); Fe-S alloy–$MgSiO_3$ (diamonds). Previous results from experiments by Bouhifd, Jephcoat, et al. (2013) and Matsuda et al. (1993), and simulations by Y. Zhang and Yin (2012) and Xiong et al. (2021) are shown as small symbols with border colors representing temperatures/pressures.

liquid. The enhanced thermodynamic stability of He in iron sulfide compared to pure iron is further supported by–after the majority of He atoms enter the silicate–a few He atoms continuing to exchange between the silicate and sulfide melt as reflected by the large fluctuation of the atom number profiles ($t > 20$ ps in Figure 1d). The square root of MSD for He atoms at the end of the simulation period (~12 Å) is comparable to or larger than the dimension of each phase (11 Å; *cf.* Table S1 for details of cell lengths), supporting the notion that the dynamics of He atoms is sufficiently fast to allow diffusive movement through the space occupied by the metallic and silicate phases.

3.2. Phase Separation of He in Molten Iron

We find that He atoms in pure liquid iron readily coalesce into a cluster (Figure S4a), which is also reflected by a broad shoulder following the first-shell peak (~1.7 Å) in the He–He radial distribution function $g_{\mathrm{HeHe}}(r)$ which for larger r tends to zero (Figure S4b). This is the case for all simulations in the Fe–He system, irrespective of starting condition and concentration of He. We find that this phenomenon persists in other metallic compositions ($Fe_{40}O_{10}$ and $Fe_{45}S_5$ alloys). Similar demixing has been described in the Fe–Ar system by Ostanin et al. (2006).

Such phase separation is unexpected, as interfaces between two phases are not stable in a small system (Hong & Van De Walle, 2013), typical for regular DFT-MD simulations. Previous simulations on the immiscibility of He–H mixtures (Lorenzen et al., 2011) demonstrated that phase separation can be observed directly only in an extremely large simulation box (512 He and 1024 H atoms). In two-phase simulations starting with separate phases, the system will often turn into a pure state (solid or liquid) (e.g., Schwegler et al., 2008) or into a homogenous mixture (e.g., Huang et al., 2019), and never return to two separate phases–even when experiments indicate that two phases are stably coexisting. The phase separations of He–Fe presented here and Ar–Fe in Ostanin et al. (2006) directly illustrate the unusually low solubility of noble gases in liquid Fe, providing a rationale for strong partitioning of He into silicates, as observed in two-phase simulations.

As a consequence of Fe–He demixing, calculations of Gibbs energy using Fe supercells that contain too many He atoms may suffer from drawbacks as any first-order phase transition along the integration path must be avoided in thermodynamic integration calculations (Frenkel & Smit, 1996). We thus include a single He atom only in each phase involved in reactions 1a–c, naturally avoiding clustering.

3.3. Partition Coefficients

Gibbs energies $G(P, T)$ for the eight compositions in reactions 1a–c ($(MgSiO_3)_{15}$, Fe_{50}, $Fe_{40}O_{10}$ $Fe_{45}S_5$, $(MgSiO_3)_{15}$He, Fe_{50}He, $Fe_{40}O_{10}$He, $Fe_{45}S_5$He) at six P–T conditions (10 GPa and 3,000 K, 25 GPa and 3,500 K, 40 GPa and 3,800 K, 50 GPa and 4,000 K, 80 GPa and 4,000 K, and 130 GPa and 5,000 K) are computed using DFT-MD combined with thermodynamic integration. To obtain $G(P, T)$ at each P–T–composition condition, seven DFT-MD simulations are conducted with different coupling constants (λ). Thermodynamic parameters corresponding to different He partitioning conditions are summarized in Table S2 in Supporting Information S1.

With G and $\Delta_r G$ for the He exchange reactions, $D^{m/s}$ can be readily calculated by solving Equation 2. $D^{m/s}$ are plotted in Figure 2a as a function of P together with previous results from experiments (Bouhifd, Jephcoat, et al., 2013; Matsuda et al., 1993) and simulations (Xiong et al., 2021; Y. Zhang & Yin, 2012). We find that He generally becomes more compatible with metal with increasing P–T: $\log_{10} D^{m/s}$ for Fe–$MgSiO_3$, Fe-S alloy–$MgSiO_3$, and Fe-O alloy–$MgSiO_3$ is −4.73 (±0.40), −4.39 (±0.33), and −2.79 (±0.32), respectively, at low P–T (10 GPa and 3,000 K), but increases to −1.24 (±0.20), −1.55 (±0.23), and −0.22 (±0.17) at high P–T (130 GPa

and 5,000 K). These results indicate that He is always lithophile at the *P–T* conditions relevant for the deep mantle, but it is approximately two orders of magnitude less lithophile at deep magma ocean conditions (40–50 GPa and 3,800–4,000 K) compared to results at lower *P–T* (10 GPa and 3,000 K).

It is important to note that Figure 2a reflects a combined effect of *P* and *T* on $D^{m/s}$ as we simultaneously change *P* and *T* following an adiabatic magma ocean profile (Figure S1). To distinguish *P* and *T* effects, we consider the Gibbs energy change ($\Delta_r G$) that drives He exchange between silicate and metal. $\Delta_r G$ can be broken down into three contributions (e.g., Wahl & Militzer, 2015): (i) A $\Delta_r U$ term from the potential energy, (ii) a $P\Delta_r V$ term from the volume difference, and (iii) a $-T\Delta_r S$ entropic term. The $P\Delta_r V$ term is negligible as the partial molar volumes of He in metallic and silicate melts are indistinguishable within uncertainties (Figure S5). Therefore the variation of $D^{m/s}$ in Figure 2a is mainly controlled by *T* rather than *P*. A recent computational study (Xiong et al., 2021) also suggested a negligible *P* effect on $D^{m/s}$. The *T* effect can be seen in Figure 2b: $D^{m/s}$ increases approximately by three orders of magnitude from 3,000 to 5,000 K for all metallic compositions of this study. A similar *T* effect was also reported in a previous DFT-MD study (Xiong et al., 2018) which has shown potassium iron–silicate partition coefficient varies by three orders of magnitude from 3,000 to 5,000 K. Given the strong *T* effect and that the *P–T* conditions in our study follow the temperature profile of a magma ocean (Figure S1), our results may be more relevant to represent metal–silicate fractionation of He during planetary accretion and differentiation than the results of DFT-MD simulations from Xiong et al. (2021) at 5,000 K and experiments from Bouhifd, Jephcoat, et al. (2013) over a limited *P* and *T* range.

We find that the presence of light elements, particularly oxygen, promotes He incorporation into the core: $D^{m/s}$ for Fe-O alloy–$MgSiO_3$ are one to two orders of magnitude larger than that for Fe–$MgSiO_3$. The two-phase simulation seems to amplify the effect of sulfur as it suggests enhanced He partitioning into the metal, whereas quantitative results from Gibbs energy calculations show that sulfur only leads to a slight increase in $D^{m/s}$. This discrepancy is probably due to the specifics of the two-phase approach. In particular, determining the interface between two phases is nontrivial, but critical as a He atom in the interface region can be assigned to either the metal or the silicate. A two-phase simulation can, in our opinion, only be used to qualitatively consider partitioning, and not to quantify a partition coefficient.

$D^{m/s}$ from earlier high *P–T* experiments by Matsuda et al. (1993) agrees with that in Bouhifd, Jephcoat, et al. (2013) at ~6 GPa, but $D^{m/s}$ determined by the former are larger (by one to two orders of magnitude) than those measured by the latter at low *P* (<6 GPa). Although pure Fe and FeNiCo metals were used as starting materials in Bouhifd, Jephcoat, et al. (2013), light elements from silicates (e.g., O, Si, and Mg) and from diamond anvils (i.e., carbon) might have migrated into the metal at high *T*. This inference is supported by (i) chemical reactions between metal and silicate observed by DAC experiments (Badro et al., 2016; Knittle & Jeanloz, 1991; Takafuji et al., 2005) which have shown that the metals contain variable amounts of Si and O, and (ii) the presence of iron carbides (Fe_7C_3 and FeC_3) after lasing heating of iron in DACs (Frost et al., 2010; Tateno et al., 2010) as a result of carbon contamination from diamond anvils (Aprilis et al., 2019; Prakapenka et al., 2003; Rouquette et al., 2008). Therefore, it may be more appropriate to compare experimental data with $D^{m/s}$ for Fe-O alloy–$MgSiO_3$ rather than Fe–$MgSiO_3$, and the calculated $D^{m/s}$ at 10 GPa for the Fe-O alloy–$MgSiO_3$ system determined here agrees well with the experimental data.

Using DFT-MD, Xiong et al. (2021) calculated $D^{m/s}$ between pure iron and silicate ($MgSiO_3$) melts at three pressures (*P* = 20 GPa, 60 GPa, and 135 GPa) and a single temperature (*T* = 5,000 K). Our results agree with theirs at a similar *P–T* condition: $\log_{10} D^{m/s} = -1.8$ at 135 GPa and 5,000 K in their work versus −1.2 at 130 GPa and 5,000 K in our study. Xiong et al. (2021) compared their low-*P* results computed at 5,000 K to experimental data (Bouhifd, Jephcoat, et al., 2013) which, however, were obtained at substantially lower *T* (<2,600 K). As we have already discussed that $D^{m/s}$ strongly depends on *T* and melt compositions, a good agreement between experimental data obtained at *T* < 2,600 K and their DFT-MD results computed at 5,000 K using pure Fe should not be overinterpreted.

Y. Zhang and Yin (2012) quantified $D^{m/s}$ at 3,200 K and 40 GPa using DFT-based two-phase simulations, and estimated $D^{m/s}$ is one order of magnitude larger than we do here for Fe–$MgSiO_3$, but their results are within the range of those we predict for Fe-O alloy–$MgSiO_3$. The discrepancy is likely caused by (i) the incorporation of light elements into metal in the two-phase models of Y. Zhang and Yin (2012) and consequently that the metal cannot be viewed as pure Fe and (ii) large uncertainties exist in two-phase approaches, which is reflected by

conflicting results on hydrogen partitioning from the study of Y. Zhang and Yin (2012) and a more robust method (Gibbs energy calculations) in Li et al. (2020).

3.4. Reactivity of He in Metallic Melts

To understand the variation of $D^{m/s}$ over metallic compositions (pure Fe, Fe-O, and Fe-S alloys), we analyze $g(r)$ between He and other atomic species. There is a noticeable difference in the height (h) of the first peak in $g(r)$ with a sequence: $h_{g_{\mathrm{HeO}}(r)} > h_{g_{\mathrm{HeS}}(r)} > h_{g_{\mathrm{HeFe}}(r)}$ (Figure S6). We further explore the electronic structure to investigate whether He forms any chemical interaction with the neighboring atoms in the metallic phases for which we perform electronic structure calculations with a denser k-point grid ($4 \times 4 \times 4$). Results are averaged over 250 uncorrelated configurational snapshots extracted from each DFT-MD trajectory:

(i) We characterize the bonding feature using the electron localization function (ELF) (Becke & Edgecombe, 1990). The ELF describes the pairing of electrons which gives information about the occurrence of covalent bonds and filled lone pairs; values close to one indicate strong covalent bonds. The He atom essentially exhibits a spherical ELF distribution (Figure S7a) and there are no local ELF maxima along the directions He–Fe, He–O, and He–S, ruling out covalent interactions between He and other species.

(ii) We examine the charge transfer based on Bader's topological analysis of the electron density (Bader, 1985). Bader charge analysis suggests a negligible charge transfer from the metallic aggregates to the He atom (Fe_{50}: 0.13 e^-; $Fe_{40}O_{10}$: 0.09 e^-; and $Fe_{45}S_5$: 0.13 e^-) (Table S3), comparable to those in Na_2He (Dong et al., 2017), FeO_2He (J. Zhang et al., 2018), MgF_2He (Z. Liu et al., 2018), NH_3–He (Shi et al., 2020), H_2O–He (H. Liu et al., 2015), and HeN_4 (Li et al., 2018) where the He atom does not form any local chemical bonds (i.e., keeps its inertness) but rather is located between like-charged ions to shield their repulsive Coulomb interactions.

(iii) We compute the projected electronic density of states (pDOS) to confirm the inertness of He in these metallic phases. We compare the two pDOSs for each phase with and without the He atom (Figure S7b). This method is similar to that used in a previous study (J. Liu et al., 2018) to quantify He reactivity in solid compounds. The He-1s states are mostly located at −20 to −15 eV and have negligible overlap with the O-2p and Fe-3d states. More importantly, the inclusion of He in the metallic structures involves the little redistribution of the electronic states of Fe, O, and S. This suggests that there is no orbital hybridization and no chemical reaction between He and the host phases.

The difference in the height of the first peak in $g_{\mathrm{HeO}}(r)$, $g_{\mathrm{HeS}}(r)$ and $g_{\mathrm{HeFe}}(r)$ (Figure S6) can therefore not be explained by local bonding around He due to its very stable closed valence shell and extremely high ionization potential. The strong first peak in $g_{\mathrm{HeO}}(r)$ may be linked to the ionic character of O in the metallic phase: Oxygen is the most highly charged species (Table S3) and the stronger repulsive Coulomb forces between O–O pairs can be shielded by He insertion. To confirm this hypothesis, future work is required to explore how the solubility of He in melts changes over a wide range of melt ionicity.

4. Discussion

4.1. Availability of He During Core Formation

The amount of He sequestered into the core strongly depends on its availability in the early Earth. While the major element composition of a magma ocean can be approximated by that of Earth's primitive mantle–estimated from the analysis of natural samples, i.e., upper mantle rocks and/or meteorites (Javoy et al., 2010; McDonough & Sun, 1995; Palme & O'Neill, 2013) –, constraining its volatile content is challenging. It requires knowledge of volatile solubility, partitioning, and an appropriate theoretical understanding of the processes of accretion and differentiation (Hirschmann, 2016). The initial concentration of He is consequently model-dependent. We examine three popular models – (i) nebular ingassing, (ii) late-stage delivery, and (iii) wet accretion–that have been proposed to explain the origin of Earth's He:

(i) The nebular ingassing model (Olson and Sharp, 2018, 2019, 2018; Sharp, 2017) suggests an origin of Earth's water and noble gas (particularly ^3He) budget through the interaction between an early atmosphere–gas gravitationally captured from the nebula (Hayashi et al., 1979; Ikoma & Genda, 2006; Saito & Kuramoto, 2018; Stökl et al., 2015) – and the magma ocean below. However, the median lifetime of the solar nebula

(~2 Myr) is significantly shorter than that for the main growth stage of Earth (~10 Myr) (Yin et al., 2002). Consequently, nebular ingassing should have mainly occurred at the embryo stage and therefore may have been inefficient (Jaupart et al., 2017), as illustrated by a predicted Ne-budget that is too small to account for the present-day Ne-content of Earth's mantle. Similarly, He would not be present in a significant amount.

(ii) The volatile-rich late-stage delivery scenario (late veneer) argues that a large proportion of volatile elements was added during (or even after) the final stages of core formation (Albarède, 2009; Wang & Becker, 2013). This scenario was originally proposed to explain the excess of highly siderophile (HSE: Os, Ir, Ru, Rh, Pt, Pd, Re, Au) (Chou et al., 1983) and moderately volatile siderophile and chalcogen elements (S, Se, Te, and Pb) (Albarède, 2009; Ballhaus et al., 2013; Wang & Becker, 2013) in the bulk silicate Earth (BSE). Astrophysical models (e.g., the "Grand Tack" scenario) support the late delivery of volatiles from the outer solar system due to the inward and outward migrations of Jupiter and Saturn (O'Brien et al., 2014; Walsh et al., 2011). In the late veneer hypothesis, however, He (and other volatiles) cannot be incorporated into the core at a significant level as they are not present during core–mantle segregation.

(iii) The wet accretion model suggests that Earth's volatile budget has been delivered as part of general accretion (e.g., Drake & Righter, 2002), with the building blocks still represented in the solar system as meteorites. The isotopic composition of Earth–including the deuterium to hydrogen (D/H) ratio (Piani et al., 2020) – suggests that it is composed of a large fraction of enstatite chondrites (Dauphas, 2017; Javoy et al., 2010). Piani et al. (2020) also found that enstatite chondrites contain far more H than is commonly assumed, with two mechanisms providing a rationale for a high volatile content: A gas-rich, nebular environment has been directly observed within one astronomical unit of the young star MWC 480 (Eisner, 2007), and dust grains exposed to solar wind irradiation may incorporate solar wind ions (primarily H^+ and He^{2+}), with penetration or implantation depths of a few hundred nanometers, depending on the energy of the incident ions (Ballentine et al., 2005; Jaupart et al., 2017; Moreira & Charnoz, 2016; Péron et al., 2017; Sasaki, 1991; Trieloff et al., 2000). Such ion implantation has been observed in lunar regoliths (Starukhina, 2006), aluminum foils exposed on the Moon during the Apollo missions (Geiss et al., 2004), and a collector exposed to the solar wind on NASA's Genesis mission (Burnett et al., 2003; Grimberg et al., 2006). Moreira and Charnoz (2016) have shown that–based on the Ne flux deduced from the Genesis targets–solar wind implantation can achieve concentrations several orders of magnitude greater than chondritic or terrestrial abundances of Ne.

Among scenarios (i) – (iii), only the wet accretion model provides sufficient He at the differentiation stage for the core to play a significant role in the He-budget of the Earth. Nevertheless, the initial He content in the early Earth is hard to estimate, also due to the degassing Earth has experienced (Moreira & Kurz, 2013). The present-day ^{3}He concentration in the mantle source of MORB is estimated to be 10^{-12} mol/kg (Moreira & Kurz, 2013) and should be much lower than the initial concentration. Following models of degassing by Coltice et al. (2011, 2009), we explore a wide range of initial concentrations of ^{3}He in the mantle, 10^{-11} – 10^{-9} mol/kg (~10–1,000 times MORB source), in estimating the He-budget of Earth's core.

4.2. Abundance of Primordial He in the Earth's Early Core

Using the newly derived $D^{m/s}$ values from our DFT-MD simulations, we make predictions of the primordial ^{3}He concentrations in the Earth's core. Two core formation models have often been considered to determine elemental partitioning between the core and BSE: (i) Single-stage core formation is a first-order model, which represents the average of a range of equilibrium conditions (J. Li & Agee, 1996; Siebert et al., 2012); (ii) continuous core formation considers accretion and core formation as dynamic processes, which account for the heterogeneity of accreting materials and metal–silicate equilibrium over a wide range of *P–T* conditions during planetary growth (Rubie et al., 2011; Rudge et al., 2010; Wade & Wood, 2005).

(i) For a single-stage core formation model, we use equilibration conditions of 40–50 GPa and 3,800–4,000 K (Corgne et al., 2009; Siebert et al., 2012) derived from partitioning data for siderophile elements (e.g., Ni, Co, and W) which show well-defined *P* dependence. The estimated abundance of ^{3}He in Earth's early core is in the range of 10^{-14} – 10^{-11} mol/kg using our $D^{m/s}$ values predicted at these conditions for the Fe–$MgSiO_3$ system. The He content is elevated by one order of magnitude when more oxygen is available in the metal–silicate system

(ii) For continuous core formation, we follow the framework of Rudge et al. (2010), where the Earth (with mass M) is assumed to grow dynamically, with embryo materials being added at a rate described by

$$M\left(t\right)=1-e^{-\left(t/\alpha\right)^{\beta}}. \quad (3)$$

Time $t = 0$ represents the beginning and $t = 1$ the end of accretion; α and β are timescale and shape parameters of the growth curve, respectively, and we use $\alpha = 2.0$ Myr and $\beta = 0.3$ from Rudge et al. (2010) to produce rapid accretion at early times (90% of the Earth accreted in less than 32 Myr), and slow rates later. Over the course of accretion, an embryo (assumed to be already differentiated) hits the growing Earth and the mantles merge directly. The core of the embryo takes two different routes to the core of the accreting Earth: A mass fraction $k = 0.4$ equilibrates with the Earth's mantle before sinking to the Earth's core, while the remainder $\left(1-k\right)$ directly sinks to the Earth's core. For fraction k, metal–silicate equilibration occurs at the base of a magma ocean at 1/2 Earth's evolving core–mantle boundary pressure (Rubie et al., 2015; Wade & Wood, 2005). We perform multiple sets of calculations, exploring a range of He-content in the accreting material that satisfies the initial concentrations of ^{3}He in the BSE (see Supplementary Information for details), and find 10^{-14} – 10^{-12} mol/kg of ^{3}He in the core after metal–silicate separation with the $D^{m/s}$ values predicted for Fe–$MgSiO_3$. Again, using the $D^{m/s}$ values predicted for Fe-O alloy–$MgSiO_3$ would produce one to two orders of magnitude more primordial ^{3}He in the core. With this primordial ^{3}He content and assuming an initial solar wind implanted ^{3}He/^{4}He ratio (326 R_a; Ozima & Podosek [2001]), the amount of primordial ^{4}He in the core is estimated as 10^{-10} – 10^{-6} mol/kg.

4.3. U and Th Partitioning and Radiogenic ^{4}He in the Core

The decay of U and Th nuclides continues to produce ^{4}He in all terrestrial reservoirs. Uranium and thorium are strongly lithophile at ambient conditions and have therefore been considered as virtually absent from the core (e.g., Wheeler et al., 2006). High-P experiments on metal–silicate partitioning of U and Th (Blanchard et al., 2017; Bouhifd, Andrault, et al., 2013; Boujibar et al., 2019; Chidester et al., 2017; Faure et al., 2020; Malavergne et al., 2007; Wheeler et al., 2006; Wohlers & Wood, 2015, 2017) have recently been parameterized as a function of P, T, and oxygen fugacity (f_{O_2}) by Faure et al. (2020), a model we apply in our work.

Starting with a current U content in BSE of 8.4×10^{-8} mol/kg (McDonough, 2003) and a Th/U mass ratio of 3.77 (Wipperfurth et al., 2018), we integrate back by 4.5 billion years and find an initial U and Th content in the BSE of 2.2×10^{-7} mol/kg and 4.1×10^{-7} mol/kg, respectively. With this initial budget and using f_{O_2} two log-units below the iron-wüstite buffer for magma ocean equilibration (Wood et al., 2006), we apply the model of Faure et al. (2020) directly in the continuous core-formation model and calculate a U and Th budget of Earth's core of 9.1×10^{-10} mol/kg and 1.2×10^{-8} mol/kg, respectively. These concentrations of U and Th have produced 10^{-6} mol/kg of ^{4}He over Earth's history.

This amount of radiogenic ^{4}He is significantly larger (by two orders of magnitude) than primordial ^{4}He inferred from $D^{m/s}$ values predicted for the Fe–$MgSiO_3$ system, and consequently, the core primordial ^{3}He/^{4}He ratio would have been severely diluted to less than 3 R_a. On the other hand, using $D^{m/s}$ values predicted for the Fe-O alloy–$MgSiO_3$ system, the amount of radiogenic ^{4}He is comparable to primordial ^{4}He and therefore the core maintains a high ^{3}He/^{4}He ratio ($\sim$140 R_a). This core He isotopic ratio is far larger than that of the ambient mantle (8 R_a). Thus, a minor transfer of core He to the lower mantle by core–mantle equilibration would efficiently elevate the ^{3}He/^{4}He ratio of the core–mantle boundary layer, potentially explaining the observed high ^{3}He/^{4}He ratios in OIBs.

5. Conclusions

We use density functional theory molecular dynamics to predict the metal–silicate partitioning behavior of He over a wide range of pressure, temperature, and three compositions for the forming core: Fe, Fe-S, and Fe-O alloys. We find that He always favors silicate over metallic melts which we illustrate in a straightforward way using a two-phase approach, and we quantify the metal–silicate partition coefficient ($D^{m/s}$) of He by thermodynamic integration. Helium is approximately two orders of magnitude less lithophile at deep magma ocean conditions (50 GPa and 4,000 K) compared to results at lower P–T (10 GPa and 3,000 K), and this variation is mainly

controlled by T rather than P. We find that light element species, particularly oxygen, promote He incorporation into the core by one to two orders of magnitude. By including a parameterization to experimental partitioning data on uranium and thorium (Faure et al., 2020) in core formation models to estimate the core ^{4}He budget, we find the He content of the core to be 1.0×10^{-6} mol/kg (or ∼4.2 ng/g), and determine its isotopic composition as ^{3}He/^{4}He ratio <3 R_a using $D^{m/s}$ values determined for pure Fe, but a higher ^{3}He/^{4}He ratio of ∼140 R_a using larger $D^{m/s}$ values determined for a core component that contains some amount of oxygen. To explain the Earth's core density deficit–which has been constrained to be larger than previous estimates (Ikuta et al., 2021) – oxygen is required as a major light element in the core (Badro et al., 2014). Thus, our results suggest that the core possibly retains a high primordial ^{3}He/^{4}He, potentially accounting for the high ^{3}He/^{4}He ratios identified in ocean island basalts.

Data Availability Statement

Simulation files supporting this study are described in methods and are archived in Figshare (10.6084/m9.figshare.16415934). All computations in this study were carried out using the Vienna *ab initio* simulation package (VASP) which is available for licensing at https://www.vasp.at/.

Acknowledgments
This work is supported by Deutsche Forschungsgemeinschaft (German Science Foundation, DFG) with grants STE1105/12-1 and STE1105/13-2 to G.S.N. Computations were performed at the Leibniz Supercomputing Center of the Bavarian Academy of Sciences and the Humanities, and the research center for scientific computing at the University of Bayreuth. L.Y. has been funded by Bayerisches Geoinstitut for his postdoctoral research. Open access funding enabled and organized by Projekt DEAL.

References

Albarède, F. (2008). Rogue mantle helium and neon. *Science*, *319*, 943–945. https://doi.org/10.1126/science.1150060
Albarède, F. (2009). Volatile accretion history of the terrestrial planets and dynamic implications. *Nature*, *461*, 1227–1233. https://doi.org/10.1038/nature08477
Alfè, D. (2005). Melting curve of MgO from first-principles simulations. *Physical Review Letters*, *94*, 235701. https://doi.org/10.1103/PhysRevLett.94.235701
Alfè, D. (2009). Temperature of the inner-core boundary of the Earth: Melting of iron at high pressure from first-principles coexistence simulations. *Physical Review B: Condensed Matter*, *79*, 060101. https://doi.org/10.1103/PhysRevB.79.060101
Alfè, D., Gillan, M. J., & Price, G. D. (2000). Constraints on the composition of the Earth's core from ab initio calculations. *Nature*, *405*, 172–175. https://doi.org/10.1038/35012056
Allègre, C. J., Staudacher, T., Sarda, P., & Kurz, M. D. (1983). Constraints on evolution of Earth's mantle from rare gas systematics. *Nature*, *303*, 762–766. https://doi.org/10.1038/303762a0
Aprilis, G., Kantor, I., Kupenko, I., Cerantola, V., Pakhomova, A., Collings, I. E., et al. (2019). Comparative study of the influence of pulsed and continuous wave laser heating on the mobilization of carbon and its chemical reaction with iron in a diamond anvil cell. *Journal of Applied Physics*, *125*, 095901. https://doi.org/10.1063/1.5067268
Arevalo, R., & McDonough, W. F. (2008). Tungsten geochemistry and implications for understanding the Earth's interior. *Earth and Planetary Science Letters*, *272*, 656–665. https://doi.org/10.1016/j.epsl.2008.05.031
Bader, R. F. W. (1985). Atoms in molecules. *Accounts of Chemical Research*, *18*, 9–15. https://doi.org/10.1021/ar00109a003
Badro, J., Côté, A. S., & Brodholt, J. P. (2014). A seismologically consistent compositional model of Earth's core. *Proceedings of the National Academy of Sciences USA*, *111*, 7542–7545. https://doi.org/10.1073/pnas.1316708111
Badro, J., Siebert, J., & Nimmo, F. (2016). An early geodynamo driven by exsolution of mantle components from Earth's core. *Nature*, *536*, 326–328. https://doi.org/10.1038/nature18594
Ballentine, C. J., Marty, B., Sherwood Lollar, B., & Cassidy, M. (2005). Neon isotopes constrain convection and volatile origin in the Earth's mantle. *Nature*, *433*, 33–38. https://doi.org/10.1038/nature03182
Ballhaus, C., Laurenz, V., Münker, C., Fonseca, R. O. C., Albarède, F., Rohrbach, A., et al. (2013). The U/Pb ratio of the Earth's mantle-A signature of late volatile addition. *Earth and Planetary Science Letters*, *362*, 237–245. https://doi.org/10.1016/j.epsl.2012.11.049
Becke, A. D., & Edgecombe, K. E. (1990). A simple measure of electron localization in atomic and molecular systems. *The Journal of Chemical Physics*, *92*, 5397–5403. https://doi.org/10.1063/1.458517
Blanchard, I., Siebert, J., Borensztajn, S., & Badro, J. (2017). The solubility of heat-producing elements in Earth's core. *Geochemical Perspective Letters*, *5*, 1–5. https://doi.org/10.7185/geochemlet.1737
Bouhifd, M. A., Andrault, D., Bolfan-Casanova, N., Hammouda, T., & Devidal, J. L. (2013). Metal-silicate partitioning of Pb and U: Effects of metal composition and oxygen fugacity. *Geochimica Cosmochimica Acta*, *114*, 13–28. https://doi.org/10.1016/j.gca.2013.03.034
Bouhifd, M. A., Jephcoat, A. P., Heber, V. S., & Kelley, S. P. (2013). Helium in Earth's early core. *Nature Geoscience*, *6*, 982–986. https://doi.org/10.1038/ngeo1959
Boujibar, A., Habermann, M., Righter, K., Ross, D. K., Pando, K., Righter, M., et al. (2019). U, Th, and K partitioning between metal, silicate, and sulfide and implications for Mercury's structure, volatile content, and radioactive heat production. *American Mineralogist*, *104*, 1221–1237. https://doi.org/10.2138/am-2019-7000
Brandon, A. D., Walker, R. J., Morgan, J. W., Norman, M. D., & Prichard, H. M. (1998). Coupled ^{186}Os and ^{187}Os evidence for core-mantle interaction. *Science*, *280*, 1570–1573. https://doi.org/10.1126/science.280.5369.1570
Burnard, P. G., Demouchy, S., Delon, R., Arnaud, N. O., Marrocchi, Y., Cordier, P., & Addad, A. (2015). The role of grain boundaries in the storage and transport of noble gases in the mantle. *Earth and Planetary Science Letters*, *430*, 260–270. https://doi.org/10.1016/j.epsl.2015.08.024
Burnett, D. S., Barraclough, B. L., Bennett, R., Neugebauer, M., Oldham, L. P., Sasaki, C. N., et al. (2003). The Genesis Discovery mission: Return of solar matter to Earth. *Space Science Reviews*, *105*, 509–534. https://doi.org/10.1023/A:1024425810605
Chidester, B. A., Rahman, Z., Righter, K., & Campbell, A. J. (2017). Metal–silicate partitioning of U: Implications for the heat budget of the core and evidence for reduced U in the mantle. *Geochimica Cosmochimica Acta*, *199*, 1–12. https://doi.org/10.1016/j.gca.2016.11.035
Chou, C. L., Shaw, D. M., & Crocket, J. H. (1983). Siderophile trace elements in the Earth's oceanic crust and upper mantle. *Journal of Geophysical Research*, *88*, A507. https://doi.org/10.1029/JB088iS02p0A507

Coltice, N., Marty, B., & Yokochi, R. (2009). Xenon isotope constraints on the thermal evolution of the early Earth. *Chemical Geology*, *266*, 4–9. https://doi.org/10.1016/j.chemgeo.2009.04.017

Coltice, N., Moreira, M., Hernlund, J., & Labrosse, S. (2011). Crystallization of a basal magma ocean recorded by Helium and Neon. *Earth and Planetary Science Letters*, *308*, 193–199. https://doi.org/10.1016/j.epsl.2011.05.045

Coltice, N., & Ricard, Y. (1999). Geochemical observations and one layer mantle convection. *Earth and Planetary Science Letters*, *174*, 125–137. https://doi.org/10.1016/S0012-821X(99)00258-7

Corgne, A., Siebert, J., & Badro, J. (2009). Oxygen as a light element: A solution to single-stage core formation. *Earth and Planetary Science Letters*, *288*, 108–114. https://doi.org/10.1016/j.epsl.2009.09.012

Dauphas, N. (2017). The isotopic nature of the Earth's accreting material through time. *Nature*, *541*, 521–524. https://doi.org/10.1038/nature20830

Dong, X., Oganov, A. R., Goncharov, A. F., Stavrou, E., Lobanov, S., Saleh, G., et al. (2017). A stable compound of helium and sodium at high pressure. *Nature Chemistry*, *9*, 440–445. https://doi.org/10.1038/nchem.2716

Dorner, F., Sukurma, Z., Dellago, C., & Kresse, G. (2018). Melting Si: Beyond density functional theory. *Physical Review Letters*, *121*, 195701. https://doi.org/10.1103/PhysRevLett.121.195701

Drake, M. J., & Righter, K. (2002). Determining the composition of the Earth. *Nature*, *416*, 39–44. https://doi.org/10.1038/416039a

Eisner, J. A. (2007). Water vapour and hydrogen in the terrestrial-planet-forming region of a protoplanetary disk. *Nature*, *447*, 562–564. https://doi.org/10.1038/nature05867

Farley, K. A., & Neroda, E. (1998). Noble gases in the Earth's mantle. *Annual Review of Earth and Planetary Sciences*, *26*, 189–218. https://doi.org/10.1146/annurev.earth.26.1.189

Faure, P., Bouhifd, M. A., Boyet, M., Manthilake, G., Clesi, V., & Devidal, J.-L. (2020). Uranium and thorium partitioning in the bulk silicate Earth and the oxygen content of Earth's core. *Geochimica Cosmochimica Acta*, *275*, 83–98. https://doi.org/10.1016/j.gca.2020.02.010

Frenkel, D., & Smit, B. (1996). *Understanding molecular simulation: From algorithms to applications, Understanding molecular simulation: From algorithms to applications*. Academic Press. https://doi.org/10.1063/1.881812

Frost, D. J., Asahara, Y., Rubie, D. C., Miyajima, N., Dubrovinsky, L. S., Holzapfel, C., et al. (2010). Partitioning of oxygen between the Earth's mantle and core. *Journal of Geophysical Research*, *115*, B02202. https://doi.org/10.1029/2009JB006302

Geiss, J., Bühler, F., Cerutti, H., Eberhardt, P., Filleux, C., Meister, J., & Signer, P. (2004). The Apollo SWC experiment: Results, conclusions, consequences. *Space Science Reviews*, *110*, 307–335. https://doi.org/10.1023/B:SPAC.0000023409.54469.40

Graham, D. W. (2002). Noble gas isotope geochemistry of mid-ocean ridge and ocean island basalts: Characterization of mantle source reservoirs. *Reviews in Mineralogy and Geochemistry*, *47*, 247–317. https://doi.org/10.2138/rmg.2002.47.8

Grimberg, A., Baur, H., Bochsler, P., Buhler, F., Burnett, D. S., Hays, C. C., et al. (2006). Solar wind neon from Genesis: Implications for the Lunar noble gas record. *Science*, *314*, 1133–1135. https://doi.org/10.1126/science.1133568

Hart, S. R., Hauri, E. H., Oschmann, L. A., & Whitehead, J. A. (1992). Mantle plumes and entrapment: Isotopic evidence. *Science*, *256*, 517–520. https://doi.org/10.1126/science.256.5056.517

Hayashi, C., Nakazawa, K., & Mizuno, H. (1979). Earth's melting due to the blanketing effect of the primordial dense atmosphere. *Earth and Planetary Science Letters*, *43*, 22–28. https://doi.org/10.1016/0012-821X(79)90152-3

He, X., Zhu, Y., Epstein, A., & Mo, Y. (2018). Statistical variances of diffusional properties from ab initio molecular dynamics simulations. *npj Computational Materials*, *4*, 18. https://doi.org/10.1038/s41524-018-0074-y

Herzberg, C., Asimow, P. D., Ionov, D. A., Vidito, C., Jackson, M. G., & Geist, D. (2013). Nickel and helium evidence for melt above the core–mantle boundary. *Nature*, *493*, 393–397. https://doi.org/10.1038/nature11771

Hirschmann, M. M. (2016). Constraints on the early delivery and fractionation of Earth's major volatiles from C/H, C/N, and C/S ratios. *American Mineralogist*, *101*, 540–553. https://doi.org/10.2138/am-2016-5452

Hong, Q. J., & Van De Walle, A. (2013). Solid-liquid coexistence in small systems: A statistical method to calculate melting temperatures. *The Journal of Chemical Physics*, *139*, 094114. https://doi.org/10.1063/1.4819792

Hoover, W. G. (1985). Canonical dynamics: Equilibrium phase-space distributions. *Physical Review A*, *31*, 1695–1697. https://doi.org/10.1103/PhysRevA.31.1695

Huang, D., Badro, J., Brodholt, J., & Li, Y. (2019). Ab initio molecular dynamics investigation of molten Fe–Si–O in Earth's core. *Geophysical Research Letters*, *46*, 6397–6405. https://doi.org/10.1029/2019GL082722

Humayun, M. (2004). Geochemical evidence for excess iron in the mantle beneath Hawaii. *Science*, *306*, 91–94. https://doi.org/10.1126/science.1101050

Ikoma, M., & Genda, H. (2006). Constraints on the mass of a habitable planet with water of nebular origin. *The Astrophysical Journal*, *648*, 696–706. https://doi.org/10.1086/505780

Ikuta, D., Ohtani, E., Fukui, H., Sakamaki, T., Ishikawa, D., & Baron, A. Q. R. (2021). Large density deficit of Earth's core revealed by a multi-megabar primary pressure scale. http://arxiv.org/abs/2104.02076

Jackson, M. G., Carlson, R. W., Kurz, M. D., Kempton, P. D., Francis, D., & Blusztajn, J. (2010). Evidence for the survival of the oldest terrestrial mantle reservoir. *Nature*, *466*, 853–856. https://doi.org/10.1038/nature09287

Jaupart, E., Charnoz, S., & Moreira, M. (2017). Primordial atmosphere incorporation in planetary embryos and the origin of Neon in terrestrial planets. *Icarus*, *293*, 199–205. https://doi.org/10.1016/j.icarus.2017.04.022

Javoy, M., Kaminski, E., Guyot, F., Andrault, D., Sanloup, C., Moreira, M., et al. (2010). The chemical composition of the Earth: Enstatite chondrite models. *Earth and Planetary Science Letters*, *293*, 259–268. https://doi.org/10.1016/j.epsl.2010.02.033

van Keken, P. E., Hauri, E. H., & Ballentine, C. J. (2002). Mantle mixing: The generation, preservation, and destruction of chemical heterogeneity. *Annual Review of Earth and Planetary Sciences*, *30*, 493–525. https://doi.org/10.1146/annurev.earth.30.091201.141236

Kellogg, L. H., Hager, B. H., & Van Der Hilst, R. D. (1999). Compositional stratification in the deep mantle. *Science*, *283*, 1881–1884. https://doi.org/10.1126/science.283.5409.1881

Knittle, E., & Jeanloz, R. (1991). Earth's core-mantle boundary: Results of experiments at high pressures and temperatures. *Science*, *251*, 1438–1443. https://doi.org/10.1126/science.251.5000.1438

Kresse, G., & Furthmüller, J. (1996). Efficient iterative schemes for ab initio total-energy calculations using a plane-wave basis set. *Physical Review B: Condensed Matter*, *54*, 11169–11186. https://doi.org/10.1103/PhysRevB.54.11169

Kresse, G., & Hafner, J. (1993). *Ab initio* molecular dynamics for liquid metals. *Physical Review B: Condensed Matter*, *47*, 558–561. https://doi.org/10.1103/PhysRevB.47.558

Kurz, M. D., Jenkins, W. J., & Hart, S. R. (1982). Helium isotopic systematics of oceanic islands and mantle heterogeneity. *Nature*, *297*, 43–47. https://doi.org/10.1038/297043a0

Kurz, M. D., Jenkins, W. J., Hart, S. R., & Clague, D. (1983). Helium isotopic variations in volcanic rocks from Loihi Seamount and the Island of Hawaii. *Earth and Planetary Science Letters*, *66*, 388–406. https://doi.org/10.1016/0012-821X(83)90154-1

Li, J., & Agee, C. B. (1996). Geochemistry of mantle-core differentiation at high pressure. *Nature*, *381*, 686–689. https://doi.org/10.1038/381686a0
Li, M., & McNamara, A. K. (2013). The difficulty for subducted oceanic crust to accumulate at the Earth's core-mantle boundary. *Journal of Geophysical Research: Solid Earth*, *118*, 1807–1816. https://doi.org/10.1002/jgrb.50156
Li, Y., Feng, X., Liu, H., Hao, J., Redfern, S. A. T., Lei, W., et al. (2018). Route to high-energy density polymeric nitrogen t-N via He-N compounds. *Nature Communications*, *9*, 1–7. https://doi.org/10.1038/s41467-018-03200-4
Li, Y., Vočadlo, L., Sun, T., & Brodholt, J. P. (2020). The Earth's core as a reservoir of water. *Nature Geoscience*, *13*, 453–458. https://doi.org/10.1038/s41561-020-0578-1
Liu, H., Yao, Y., & Klug, D. D. (2015). Stable structures of He and H_2O at high pressure. *Physical Review B - Condensed Matter and Material Physics*, *91*, 014102. https://doi.org/10.1103/PhysRevB.91.014102
Liu, Z., Botana, J., Hermann, A., Valdez, S., Zurek, E., Yan, D., et al. (2018). Reactivity of He with ionic compounds under high pressure. *Nature Communications*, *9*, 1–10. https://doi.org/10.1038/s41467-018-03284-y
Lorenzen, W., Holst, B., & Redmer, R. (2011). Metallization in hydrogen-helium mixtures. *Physical Review B: Condensed Matter*, *84*, 235109. https://doi.org/10.1103/PhysRevB.84.235109
Macpherson, C. G., Hilton, D. R., Sinton, J. M., Poreda, R. J., & Craig, H. (1998). High $^3He/^4He$ ratios in the Manus backarc basin: Implications for mantle mixing and the origin of plumes in the western Pacific Ocean. *Geology*, *26*, 1007–1010. https://doi.org/10.1130/0091-7613(1998)026<1007:HHHRIT>2.3.CO;2
Malavergne, V., Tarrida, M., Combes, R., Bureau, H., Jones, J., & Schwandt, C. (2007). New high-pressure and high-temperature metal/silicate partitioning of U and Pb: Implications for the cores of the Earth and Mars. *Geochimica Cosmochimica Acta*, *71*, 2637–2655. https://doi.org/10.1016/j.gca.2007.03.011
Matsuda, J., Sudo, M., Ozima, M., Ito, K., Ohtaka, O., & Ito, E. (1993). Noble gas partitioning between metal and silicate under high pressures. *Science*, *259*, 788–790. https://doi.org/10.1126/science.259.5096.788
McDonough, W. F. (2003). Compositional model for the Earth's core. *In Treatise on Geochemistry* (pp. 547–568). Elsevier. https://doi.org/10.1016/B0-08-043751-6/02015-6
McDonough, W. F., & Sun, S.-S. (1995). The composition of the Earth. *Chemical Geology*, *120*, 223–253. https://doi.org/10.1016/0009-2541(94)00140-4
Moreira, M., & Charnoz, S. (2016). The origin of the neon isotopes in chondrites and on Earth. *Earth and Planetary Science Letters*, *433*, 249–256. https://doi.org/10.1016/j.epsl.2015.11.002
Moreira, M. A., & Kurz, M. D. (2013). Noble gases as tracers of mantle processes and magmatic degassing. *In Advances in Isotope Geochemistry* (pp. 371–391). Springer. https://doi.org/10.1007/978-3-642-28836-4_12
Mukhopadhyay, S., & Parai, R. (2019). Noble gases: A record of Earth's evolution and mantle dynamics. *Annual Review of Earth and Planetary Sciences*, *47*, 389–419. https://doi.org/10.1146/annurev-earth-053018-060238
Mundl-Petermeier, A., Touboul, M., Jackson, M. G., Day, J. M. D., Kurz, M. D., Lekic, V., et al. (2017). Tungsten-182 heterogeneity in modern ocean island basalts. *Science*, *356*, 66–69. https://doi.org/10.1126/science.aal4179
Mundl-Petermeier, A., Walker, R. J., Fischer, R. A., Lekic, V., Jackson, M. G., & Kurz, M. D. (2020). Anomalous ^{182}W in high $^3He/^4He$ ocean island basalts: Fingerprints of Earth's core? *Geochimica Cosmochimica Acta*, *271*, 194–211. https://doi.org/10.1016/j.gca.2019.12.020
Nosé, S. (1984). A unified formulation of the constant temperature molecular dynamics methods. *The Journal of Chemical Physics*, *81*, 511–519. https://doi.org/10.1063/1.447334
O'Brien, D. P., Walsh, K. J., Morbidelli, A., Raymond, S. N., & Mandell, A. M. (2014). Water delivery and giant impacts in the "Grand Tack" scenario. *Icarus*, *239*, 74–84. https://doi.org/10.1016/j.icarus.2014.05.009
Olson, P., & Sharp, Z. D. (2018). Hydrogen and helium ingassing during terrestrial planet accretion. *Earth and Planetary Science Letters*, *498*, 418–426. https://doi.org/10.1016/J.EPSL.2018.07.006
Olson, P., & Sharp, Z. D. (2019). Nebular atmosphere to magma ocean: A model for volatile capture during Earth accretion. *Physics of the Earth and Planetary Interiors*, *294*, 106294. https://doi.org/10.1016/j.pepi.2019.106294
Ostanin, S., Alfè, D., Dobson, D., Vočadlo, L., Brodholt, J. P., & Price, G. D. (2006). Ab initio study of the phase separation of argon in molten iron at high pressures. *Geophysical Research Letters*, *33*, L06303. https://doi.org/10.1029/2005GL024276
Ozima, M., & Podosek, F. A. (2001). *Noble gas Geochemistry*. Cambridge University Press. https://doi.org/10.1017/CBO9780511545986
Palme, H., & O'Neill, H. (2013). Cosmochemical estimates of mantle composition. In *Treatise on Geochemistry* (2nd ed., pp. 1–39). https://doi.org/10.1016/B978-0-08-095975-7.00201-1
Parai, R., Mukhopadhyay, S., & Standish, J. J. (2012). Heterogeneous upper mantle Ne, Ar and Xe isotopic compositions and a possible Dupal noble gas signature recorded in basalts from the Southwest Indian Ridge. *Earth and Planetary Science Letters*, *359–360*, 227–239. https://doi.org/10.1016/j.epsl.2012.10.017
Parman, S. W. (2007). Helium isotopic evidence for episodic mantle melting and crustal growth. *Nature*, *446*, 900–903. https://doi.org/10.1038/nature05691
Parman, S. W., Kurz, M. D., Hart, S. R., & Grove, T. L. (2005). Helium solubility in olivine and implications for high $^3He/^4He$ in ocean island basalts. *Nature*, *437*, 1140–1143. https://doi.org/10.1038/nature04215
Pepin, R. O., & Porcelli, D. (2002). Origin of noble gases in the terrestrial planets. *Reviews in Mineralogy and Geochemistry*, *47*, 191–246. https://doi.org/10.2138/rmg.2002.47.7%0A
Perdew, J. P., Burke, K., & Ernzerhof, M. (1996). Generalized gradient approximation made simple. *Physical Review Letters*, *77*, 3865–3868. https://doi.org/10.1103/PhysRevLett.77.3865
Péron, S., Moreira, M., Putlitz, B., & Kurz, M. D. (2017). Solar wind implantation supplied light volatiles during the frst stage of Earth accretion. *Geochemical Perspectve Letters*, *3*, 151–159. https://doi.org/10.7185/geochemlet.1718
Piani, L., Marrocchi, Y., Rigaudier, T., Vacher, L. G., Thomassin, D., & Marty, B. (2020). Earth's water may have been inherited from material similar to enstatite chondrite meteorites. *Science*, *369*, 1110–1113. https://doi.org/10.1126/science.aba1948
Porcelli, D., & Halliday, A. N. (2001). The core as a possible source of mantle helium. *Earth and Planetary Science Letters*, *192*, 45–56. https://doi.org/10.1016/S0012-821X(01)00418-6
Posner, E. S., & Steinle-Neumann, G. (2019). Mass transport and structural properties of binary liquid iron alloys at high pressure. *Geochemistry, Geophysics, Geosystems*, *20*, 3556–3568. https://doi.org/10.1029/2019GC008393
Prakapenka, V., Shen, G., & Dubrovinsky, L. (2003). Carbon transport in diamond anvil cells. *High Temperatures - High Pressures*, *35/36*, 237–249. https://doi.org/10.1068/htjr098
Puligheddu, M., & Galli, G. (2020). Atomistic simulations of the thermal conductivity of liquids. *Physical Review Materials*, *4*, 053801. https://doi.org/10.1103/PhysRevMaterials.4.053801

Puligheddu, M., Gygi, F., & Galli, G. (2017). First-principles simulations of heat transport. *Physical Review Materials*, *1*, 060802. https://doi.org/10.1103/PhysRevMaterials.1.060802

Rang, M., & Kresse, G. (2019). First-principles study of the melting temperature of MgO. *Physical Review B: Condensed Matter*, *99*, 184103. https://doi.org/10.1103/PhysRevB.99.184103

Rizo, H., Andrault, D., Bennett, N. R., Humayun, M., Brandon, A., Vlastelic, I., et al. (2019). ^{182}W evidence for core-mantle interaction in the source of mantle plumes. *Geochemical Perspective Letters*, *11*, 6–11. https://doi.org/10.7185/geochemlet.1917

Roth, A. S. G., Liebske, C., Maden, C., Burton, K. W., Schönbächler, M., & Busemann, H. (2019). The primordial He budget of the Earth set by percolative core formation in planetesimals. *Geochemical Perspective Letters*, *9*, 26–31. https://doi.org/10.7185/geochemlet.1901

Rouquette, J., Dolejš, D., Kantor, I. Y., McCammon, C. A., Frost, D. J., Prakapenka, V. B., & Dubrovinsky, L. S. (2008). Iron-carbon interactions at high temperatures and pressures. *Applied Physics Letters*, *92*, 121912. https://doi.org/10.1063/1.2892400

Rubie, D. C., Frost, D. J., Mann, U., Asahara, Y., Nimmo, F., Tsuno, K., et al. (2011). Heterogeneous accretion, composition and core–mantle differentiation of the Earth. *Earth and Planetary Science Letters*, *301*, 31–42. https://doi.org/10.1016/J.EPSL.2010.11.030

Rubie, D. C., Jacobson, S. A., Morbidelli, A., O'Brien, D. P., Young, E. D., de Vries, J., et al. (2015). Accretion and differentiation of the terrestrial planets with implications for the compositions of early-formed Solar System bodies and accretion of water. *Icarus*, *248*, 89–108. https://doi.org/10.1016/j.icarus.2014.10.015

Rudge, J. F., Kleine, T., & Bourdon, B. (2010). Broad bounds on Earth's accretion and core formation constrained by geochemical models. *Nature Geoscience*, *3*, 439–443. https://doi.org/10.1038/ngeo872

Saito, H., & Kuramoto, K. (2018). Formation of a hybrid-type proto-atmosphere on Mars accreting in the solar nebula. *Monthly Notices of the Royal Astronomical Society*, *475*, 1274–1287. https://doi.org/10.1093/mnras/stx3176

Sasaki, S. (1991). Off-disk penetration of ancient solar wind. *Icarus*, *91*, 29–38. https://doi.org/10.1016/0019-1035(91)90123-B

Sato, T., Funamori, N., & Yagi, T. (2011). Helium penetrates into silica glass and reduces its compressibility. *Nature Communications*, *2*, 1–5. https://doi.org/10.1038/ncomms1343

Scherstén, A., Elliott, T., Hawkesworth, C., & Norman, M. (2004). Tungsten isotope evidence that mantle plumes contain no contribution from the Earth's core. *Nature*, *427*, 234–237. https://doi.org/10.1038/nature02221

Schwegler, E., Sharma, M., Gygi, F., & Galli, G. (2008). Melting of ice under pressure. *Proceedings of the National Academy of Sciences USA*, *105*, 14779–14783. https://doi.org/10.1073/pnas.0808137105

Sharp, Z. D. (2017). Nebular ingassing as a source of volatiles to the terrestrial planets. *Chemical Geology*, *448*, 137–150. https://doi.org/10.1016/j.chemgeo.2016.11.018

Shen, G., Mei, Q., Prakapenka, V. B., Lazor, P., Sinogeikin, S., Meng, Y., & Park, C. (2011). Effect of helium on structure and compression behavior of SiO_2 glass. *Proceedings of the National Academy of Sciences USA*, *108*, 6004–6007. https://doi.org/10.1073/pnas.1102361108

Shi, J., Cui, W., Hao, J., Xu, M., Wang, X., & Li, Y. (2020). Formation of ammonia–helium compounds at high pressure. *Nature Communications*, *111*(11), 1–7. https://doi.org/10.1038/s41467-020-16835-z

Siebert, J., Badro, J., Antonangeli, D., & Ryerson, F. J. (2012). Metal–silicate partitioning of Ni and Co in a deep magma ocean. *Earth and Planetary Science Letters*, *321–322*, 189–197. https://doi.org/10.1016/j.epsl.2012.01.013

Starukhina, L. V. (2006). Polar regions of the moon as a potential repository of solar-wind-implanted gases. *In Advances in Space Research* (Vol. 37, pp. 50–58). Elsevier Ltd. https://doi.org/10.1016/j.asr.2005.04.033

Stökl, A., Dorfi, E., & Lammer, H. (2015). Hydrodynamic simulations of captured protoatmospheres around Earth-like planets. *Astronomy and Astrophysics*, *576*, A87. https://doi.org/10.1051/0004-6361/201423638

Stuart, F. M., Lass-Evans, S., Godfrey Fitton, J., & Ellam, R. M. (2003). High ^{3}He/^{4}He ratios in picritic basalts from Baffin Island and the role of a mixed reservoir in mantle plumes. *Nature*, *424*, 57–59. https://doi.org/10.1038/nature01711

Takafuji, N., Hirose, K., Mitome, M., & Bando, Y. (2005). Solubilities of O and Si in liquid iron in equilibrium with (Mg,Fe)SiO_3 perovskite and the light elements in the core. *Geophysical Research Letters*, *32*, L06313. https://doi.org/10.1029/2005GL022773

Taniuchi, T., & Tsuchiya, T. (2018). The melting points of MgO up to 4 TPa predicted based on *ab initio* thermodynamic integration molecular dynamics. *Journal of Physics: Condensed Matter*, *30*, 114003. https://doi.org/10.1088/1361-648X/aaac96

Tateno, S., Hirose, K., Ohishi, Y., & Tatsumi, Y. (2010). The structure of iron in earth's inner core. *Science*, *330*, 359–361. https://doi.org/10.1126/science.1194662

Tolstikhin, I., & Hofmann, A. W. (2005). Early crust on top of the Earth's core. *Physics of the Earth and Planetary Interiors*, *148*, 109–130. https://doi.org/10.1016/j.pepi.2004.05.011

Trieloff, M., & Kunz, J. (2005). Isotope systematics of noble gases in the Earth's mantle: Possible sources of primordial isotopes and implications for mantle structure. *Physics of the Earth and Planetary Interiors*, *148*, 13–38. https://doi.org/10.1016/j.pepi.2004.07.007

Trieloff, M., Kunz, J., Clague, D. A., Harrison, D., & Allègre, C. J. (2000). The nature of pristine noble gases in mantle plumes. *Science*, *288*, 1036–1038. https://doi.org/10.1126/science.288.5468.1036

Usui, Y., & Tsuchiya, T. (2010). Ab initio two-phase molecular dynamics on the melting curve of SiO_2. *Journal of Earth Sciences*, *21*, 801–810. https://doi.org/10.1007/s12583-010-0126-9

Van Der Hilst, R. D., Widiyantoro, S., & Engdahl, E. R. (1997). Evidence for deep mantle circulation from global tomography. *Nature*, *386*, 578–584. https://doi.org/10.1038/386578a0

Vočadlo, L., Wood, I. G., Alfè, D., & Price, G. D. (2008). Ab initio calculations on the free energy and high P–T elasticity of face-centred-cubic iron. *Earth and Planetary Science Letters*, *268*, 444–449. https://doi.org/10.1016/J.EPSL.2008.01.043

Wade, J., & Wood, B. J. (2005). Core formation and the oxidation state of the Earth. *Earth and Planetary Science Letters*, *236*, 78–95. https://doi.org/10.1016/j.epsl.2005.05.017

Wahl, S. M., & Militzer, B. (2015). High-temperature miscibility of iron and rock during terrestrial planet formation. *Earth and Planetary Science Letters*, *410*, 25–33. https://doi.org/10.1016/J.EPSL.2014.11.014

Walsh, K. J., Morbidelli, A., Raymond, S. N., O'Brien, D. P., & Mandell, A. M. (2011). A low mass for Mars from Jupiter's early gas-driven migration. *Nature*, *475*, 206–209. https://doi.org/10.1038/nature10201

Wang, Z., & Becker, H. (2013). Ratios of S, Se and Te in the silicate Earth require a volatile-rich late veneer. *Nature*, *499*, 328–331. https://doi.org/10.1038/nature12285

Wartho, J. A., Kelley, S. P., & Elphick, S. C. (2005). Estimates of Ar diffusion and solubility in leucite and nepheline: Electron microprobe imaging of Ar distribution in a mineral. *American Mineralogist*, *90*, 954–962. https://doi.org/10.2138/am.2005.1320

Watson, E. B., & Cherniak, D. J. (2003). Lattice diffusion of Ar in quartz, with constraints on Ar solubility and evidence of nanopores. *Geochimica Cosmochimica Acta*, *67*, 2043–2062. https://doi.org/10.1016/S0016-7037(02)01340-6

Wheeler, K. T., Walker, D., Fei, Y., Minarik, W. G., & McDonough, W. F. (2006). Experimental partitioning of uranium between liquid iron sulfide and liquid silicate: Implications for radioactivity in the Earth's core. *Geochimica Cosmochimica Acta*, *70*, 1537–1547. https://doi.org/10.1016/j.gca.2005.11.023

Williams, C. D., Mukhopadhyay, S., Rudolph, M. L., & Romanowicz, B. (2019). Primitive helium is sourced from seismically slow regions in the lowermost mantle. *Geochemistry, Geophysics, Geosystems*, *20*, 4130–4145. https://doi.org/10.1029/2019GC008437

Wipperfurth, S. A., Guo, M., Šrámek, O., & McDonough, W. F. (2018). Earth's chondritic Th/U: Negligible fractionation during accretion, core formation, and crust–mantle differentiation. *Earth and Planetary Science Letters*, *498*, 196–202. https://doi.org/10.1016/j.epsl.2018.06.029

Wohlers, A., & Wood, B. J. (2015). A Mercury-like component of early Earth yields uranium in the core and high mantle ^{142}Nd. *Nature*, *520*, 337–340. https://doi.org/10.1038/nature14350

Wohlers, A., & Wood, B. J. (2017). Uranium, thorium and REE partitioning into sulfide liquids: Implications for reduced S-rich bodies. *Geochimica Cosmochimica Acta*, *205*, 226–244. https://doi.org/10.1016/j.gca.2017.01.050

Wood, B. J., Walter, M. J., & Wade, J. (2006). Accretion of the Earth and segregation of its core. *Nature*, *441*, 825–833. https://doi.org/10.1038/nature04763

Xiao, B., & Stixrude, L. (2018). Critical vaporization of $MgSiO_3$. *Proceedings of the National Academy of Sciences USA*, *115*, 5371–5376. https://doi.org/10.1073/pnas.1719134115

Xiong, Z., Tsuchiya, T., & Taniuchi, T. (2018). Ab initio prediction of potassium partitioning into Earth's Core. *Journal of Geophysical Research: Solid Earth*, *123*, 6451–6458. https://doi.org/10.1029/2018JB015522

Xiong, Z., Tsuchiya, T., & Van Orman, J. A. (2021). Helium and argon partitioning between liquid iron and silicate melt at high pressure. *Geophysical Research Letters*, *48*, e2020GL090769. https://doi.org/10.1029/2020gl090769

Yin, Q., Jacobsen, S. B., Yamashita, K., Blichert-Toft, J., Télouk, P., & Albarède, F. (2002). A short timescale for terrestrial planet formation from Hf–W chronometry of meteorites. *Nature*, *418*, 949–952. https://doi.org/10.1038/nature00995

Yuan, L., & Steinle-Neumann, G. (2020). Strong sequestration of hydrogen into the Earth's core during planetary differentiation. *Geophysical Research Letters*, *47*, e2020GL088303. https://doi.org/10.1029/2020GL088303

Yuan, L., Steinle-Neumann, G., & Suzuki, A. (2020). Structure and density of H_2O-rich Mg_2SiO_4 melts at high pressure from ab initio simulations. *Journal of Geophysical Research: Solid Earth*, *125*, e2020JB020365. https://doi.org/10.1029/2020JB020365

Zhang, J., Lv, J., Li, H., Feng, X., Lu, C., Redfern, S. A. T., et al. (2018). Rare helium-bearing compound FeO_2He stabilized at deep-earth conditions. *Physical Review Letters*, *121*, 255703. https://doi.org/10.1103/PhysRevLett.121.255703

Zhang, Y., & Yin, Q. Z. (2012). Carbon and other light element contents in the Earth's core based on first-principles molecular dynamics. *Proceedings of the National Academy of Sciences USA.*, *109*, 19579–19583. https://doi.org/10.1073/pnas.1203826109